Pertanika J. Sci. & Technol. 34 (5): 2545 - 2567 (2026)

PERTANIKA JOURNALS

SCIENCE & TECHNOLOGY

Journal homepage: http://www.pertanika.upm.edu.my/

Data-Driven System Identification Modelling for the Reactor TRIGA PUSPATI Using Real Operational Data

Nor Arymaswati Abdullah[1,2], Azura Che Soh[1]*, Siti Marhainis Othman[3], Ribhan Zafira Abdul Rahman[1], Samsul Bahari Mohd Noor[1], and Julia Abdul Karim[2]

[1]Department of Electrical and Electronic Engineering, Faculty of Engineering, Universiti Putra Malaysia, 43400 UPM Serdang, Selangor, Malaysia

[2]Reactor Instrumentation and Control Engineering, Reactor Technology Centre, Malaysian Nuclear Agency, Bangi, 43000 Kajang, Selangor, Malaysia

[3]Faculty of Electrical Engineering & Technology, Universiti Malaysia Perlis (UniMAP), Pauh Putra Campus, 02600 Arau, Perlis, Malaysia

ABSTRACT

Accurate reactor modelling is essential to ensure reliable system performance, particularly when equipment degradation, disturbances, and parameter variations reduce model accuracy over time. The existing model of the Reactor TRIGA PUSPATI (RTP), which is based on the First Principle (FP) approach, has experienced reduced accuracy due to ageing effects, maintenance activities, and system modifications. Therefore, this study proposes a data-driven System Identification (SI) approach using actual reactor operational input and output data to develop a more accurate reactor core subsystem model. The RTP system was divided into three subsystems, namely thermal-hydraulics, reactivity, and neutronics. SI-based models were developed and validated at three reactor power levels: 500 kW, 750 kW, and 1000 kW. The results demonstrated that the developed SI models achieved acceptable performance and accurately tracked the real reactor plant behaviour. The reactivity subsystem produced the closest representation of the actual plant, with Residual Mean Percentage (RMP) values ranging from 1.09% to 1.84%, while the thermal-hydraulics and neutronics subsystems recorded RMP values ranging from 0.69% to 27.45% and 1.28% to 31.54%, respectively. Comparative evaluation between the SI and FP models showed that the SI approach consistently produced lower residual errors and better dynamic representation of the RTP system. These findings demonstrate

ARTICLE INFO

Article history:
Received: 28 June 2026
Accepted: 05 August 2026
Published: 30 October 2026

DOI: https://doi.org/10.47836/pjst.34.5.01

E-mail addresses:
n.arymas@gmail.com (Nor Arymaswati Abdullah)
azuracs@upm.edu.my (Azura Che Soh)
marhainis@unimap.edu.my (Siti Marhainis Othman)
ribhan@upm.edu.my (Ribhan Zafira Abdul Rahman)
samsul@upm.edu.my (Samsul Bahari Mohd Noor)
julia@nm.gov.my (Julia Abdul Karim)
* Corresponding author

e-ISSN: 2231-8526

© Universiti Putra Malaysia Press

the effectiveness of the SI approach in improving the accuracy of reactor subsystem modelling using real operational data.

Keywords: Data-driven, modelling, reactor TRIGA PUSPATI (RTP), real operational data, system identification

INTRODUCTION

The ageing of research reactors has become a significant issue in many countries due to both physical and non-physical degradation, which may reduce reactor performance, efficiency, and operational reliability (Leong et al., 2015; Martón et al., 2023; Nagai et al., 2011; Ratiko et al., 2020). Ageing effects generally occur gradually over time and may lead to performance deterioration, while radiation effects can introduce rapid and unpredictable changes caused by environmental conditions (Leong et al., 2015). In research reactors, these issues may also affect operational capability and radioisotope production (Nagai et al., 2011). Consequently, accurate modelling is essential to ensure reliable system operation and precise dynamic representation of the reactor behaviour.

In industrial and reactor systems, equipment degradation, disturbances, and parameter variations can increase the mismatch between the actual plant and the developed mathematical model. Conventional FP models are commonly developed based on fundamental physical laws to represent system dynamics. Although FP models are widely used and can provide accurate results, they are often computationally complex, require extensive system knowledge, and involve many parameters. In nuclear reactor applications, FP and physics-based models such as MCNP6, REBUS MCNP6, SRAC MCNP, and RELAP have been widely used for reactor analysis and simulation (Dim & Aghara, 2019; Nguyen et al., 2020; Safaei Arshi et al., 2021). However, these models require a detailed understanding of reactor physics and system behaviour, making the modelling process difficult and time-consuming. In many cases, the mathematical model is developed during the initial reactor installation and is not updated after equipment replacement, system modifications, or ageing effects. Consequently, the existing model may no longer accurately represent the plant's actual behaviour, leading to reduced modelling accuracy and system performance.

Artificial Intelligence (AI) approaches, especially machine learning techniques such as Artificial Neural Networks (ANNs), have become increasingly popular due to their ability to learn system behaviour and model nonlinear systems (Mao et al., 2022; Melo et al., 2024; Wu et al., 2025). ANN methods have been widely used in system modelling to improve prediction and control performance. Previous studies have applied ANN to heat exchangers and closed-loop systems to improve modelling accuracy and reduce model mismatch (Aguel et al., 2019; Son et al., 2022). However, ANN models usually require large amounts of data and high computational effort. Their performance may also be affected by random

parameter initialisation, which can reduce estimation accuracy and cause convergence to local optima (Mao et al., 2022). In addition, machine learning models may have difficulty adapting to changes in system behaviour after training (Kim & Kim, 2020).

Another widely used artificial intelligence approach is fuzzy logic, which is effective for modelling systems with uncertainty, nonlinearity, and incomplete information (Tang & Ahmad, 2024). Fuzzy logic has been widely applied in process modelling and control, including chemical processes, energy systems, robotics, and industrial fault diagnosis (Mohindru, 2024). In addition, the integration of fuzzy logic with optimisation and machine learning techniques has demonstrated promising performance in soft sensing, predictive maintenance, and real-time fault detection applications, particularly in industrial environments subject to sensor noise and operational disturbances (Khalid & Khan, 2023). However, fuzzy logic models may suffer from limitations such as sensitivity to membership function design, increased computational complexity in high-dimensional systems, and reduced interpretability when combined with advanced learning algorithms. Therefore, although fuzzy logic offers strong capabilities for handling uncertain and nonlinear systems, challenges related to scalability, robustness, and computational efficiency remain.

To overcome these limitations, data-driven modelling approaches such as SI have gained considerable attention in industrial applications. SI modelling develops mathematical representations directly from measured input and output data without requiring extensive prior knowledge of the system. This approach reduces modelling complexity while maintaining satisfactory accuracy in representing dynamic system behaviour. Recent studies have shown that SI-based modelling is highly effective for complex nonlinear industrial systems due to its strong adaptability, robustness, and ability to represent dynamic processes with high accuracy (Liu et al., 2024; Wang et al., 2024; Zhang et al., 2025). Compared with AI approaches such as ANNs and fuzzy logic, SI modelling generally requires fewer parameters and does not rely heavily on extensive training or self-learning. In addition, AI-based methods may produce inconsistent or uncertain decision-making results when system operating conditions change significantly. Therefore, SI modelling remains a practical, reliable, and computationally efficient approach for dynamic system modelling in complex industrial applications.

Currently, the RTP model is developed using the FP modelling approach. Throughout its operational lifetime, the reactor has undergone various modifications, maintenance activities, and equipment replacements, which may contribute to parameter variations and reduce the accuracy of the existing reactor model. In addition to ageing effects, preventive and corrective maintenance, as well as system modifications, have been implemented. However, model accuracy has not shown significant improvement, with the reported steady-state error remaining between 0.235 and 0.7 (Ghazali et al., 2017; Minhat et al., 2018). Therefore, this study proposes developing a new reactor core subsystem model using a

data-driven SI approach based on actual operational input and output data. The proposed approach is expected to account for ageing effects and time-varying characteristics while reducing modelling complexity and improving the accuracy and dynamic representation of the RTP system.

REACTOR CORE SYSTEM

The block diagram of the reactor core system is illustrated in Figure 1. The reactor core system consists of three integrated subsystems, namely the thermal-hydraulic model, reactivity model, and neutronics model. Each subsystem generates its own corresponding model, which collectively represents the overall RTP reactor system. The inputs and outputs of these models are interdependent, except for the insertion reactivity and inlet coolant temperature. The inlet coolant temperature is assumed constant because real plant data for this parameter are unavailable.

Thermal-hydraulics Model

The thermal-hydraulics modelling for the RTP system comprises a few parameters, as shown in Figure 2. Inputs and outputs are neutron power and inlet coolant temperature, and coolant temperature and fuel temperature, respectively. The real output data from the thermal-hydraulics model comes from sensors in the RTP system. The function of the inlet

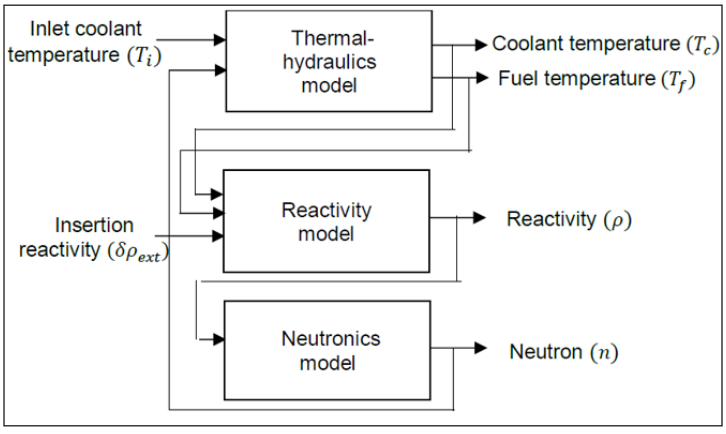

Figure 1. Block diagram of the reactor core system

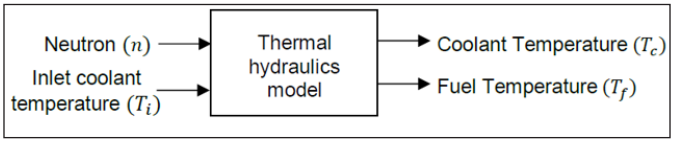

Figure 2. Thermal-hydraulics subsystem model for RTP

coolant temperature, Ti, is to dissipate heat in the reactor core, especially from the clad surface. This parameter is defined as a constant value at 32°C since there is no sensor for this variable. The neutron input is a nominal power from the neutronics model.

The temperature drop between the fuel and the coolant is compared with the temperature rise of the coolant, as expressed in Equation 1:

$$\frac{\bar{T}_f - \bar{T}_c}{\bar{T}_o - \bar{T}_i} = R_f w c_p \quad [1]$$

where c_p is the specific heat, $\bar{T}_o$ is the outlet coolant temperature, $\bar{T}_i$ is the inlet coolant temperature, R_f is the reactor core thermal resistance, and w is the coolant mass flow rate.

The dynamic variation of the coolant temperature is described by Equation 2 (Rafiei et al., 2019).

$$\frac{d}{dt}\bar{T}_c(t) = \frac{1}{\tau'}\left[\bar{T}_f(t) - \bar{T}_c(t)\right] - \frac{1}{\tau''}\left[\bar{T}_c(t) - \bar{T}_i\right]$$
$$\tau' = \frac{M_c c_p}{M_f c_f} \quad \text{and} \quad \tau'' = \frac{M_c c_p}{2\, w c_f} \quad [2]$$

where M_c is the coolant mass within the core. Nuclear fission produces heat that needs to be transferred. The temperature drop in the power reactor from fuel to coolant, which is proportional to the linear heat rate, can be described by Equation 3 (Arda & Holbert, 2016).

$$T_f(r,z) - T_c(r,z) = R_f P f_r(r) f_z(z), \quad [3]$$

where,

$$P = \frac{\bar{T}_f - \bar{T}_c}{R_f}$$

With consideration of cooling being cut off entirely, all the heat produced would result in the adiabatic heating of the fuel, as expressed in Equation 4:

$$M_f c_f \frac{d}{dt}\bar{T}_f(t) = P(t) \quad [4]$$

Where M_f and c_f are the total fuel mass and the specific heat. The approximate lumped-parameter model for thermal transients can be described by Equation 5 (Minhat et al., 2020).

$$M_f c_f \frac{d}{dt}\bar{T}_f(t) = P(t) - \frac{1}{R_f}\left[\bar{T}_f(t) - \bar{T}_c(t)\right]$$
$$\frac{d}{dt}\bar{T}_f(t) = \frac{1}{M_f c_f}P(t) - \frac{1}{\tau}\left[\bar{T}_f(t) - \bar{T}_c(t)\right] \quad [5]$$

The summarised thermal-hydraulic modelling is given by Equations 6 and 7 for the coolant and fuel temperatures, respectively (Cammi et al., 2013; Kazeminejad, 2012).

$$\frac{dT_C}{dt} = \frac{P(1-f)}{\tau_c K} + \frac{T_f - T_C}{\tau_c} - \frac{c_c}{\tau_c K w}\Gamma(T_C - T_i) \quad [6]$$

$$\frac{dT_f}{dt} = \frac{Pf}{\tau_f K} + \frac{T_f - T_C}{\tau_f} \quad [7]$$

where,

$T_C = wT_o + (1-w)T_i$ and

$$\Gamma = \sqrt{\frac{\delta_{in} g L v}{\alpha_2 w}}(T_C - T_i)$$

Where L is core height, α_2 is a factor for friction along the core channel, δ_{in} is the stationary density of the inlet water, K is the overall heat transfer coefficient between fuel and coolant, P is thermal power generated (also called actual core power) within the core volume by fission, τ_c is the time constant associated with the moderator and τ_f. The time constant is associated with the fuel.

Reactivity Model

The reactivity subsystem of the RTP consists of fuel temperature, coolant temperature, and insertion reactivity as input variables, with total reactivity as the output variable. The structure of the reactivity subsystem model is illustrated in Figure 3.

The fission chain reaction is essential for controlling the neutron population in the reactor. This behaviour is represented by the effective neutron multiplication factor, k_{eff}, which is defined in Equation 8 (Oka & Suzuki, 2013).

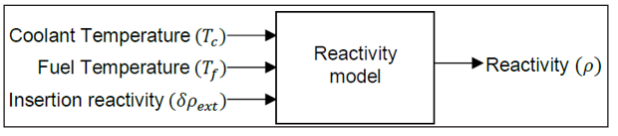

Figure 3. Reactivity subsystem model for RTP

$$k_{eff} = \frac{\text{Neutron production}}{\text{Neutron loss rate}} \quad [8]$$

where the neutron loss rate is the sum of neutron absorption and leakage rates. When $k_{eff} > 1$. The reactor is in a supercritical state, and the chain reaction increases. When $k_{eff} = 1$. The reactor is in a critical state, where the neutron population and reactor power remain constant. Meanwhile, when $k_{eff} < 1$. The reactor is subcritical, and the fission reaction decreases.

The reactor reactivity changes with the movement of the control rods and temperature variations within the reactor core. Therefore, the total reactivity can be expressed by Equation 9 (Ribeiro et al., 2020):

$$\rho(t) = \alpha_h \Delta h_{cr} + \alpha_c (T_c - T_c^0) + \alpha_f (T_f - T_f^0) \quad [9]$$

where Δh_{cr} is the extraction height of the control rod measured from the critical position, α_h is the rod worth coefficient, T_c^0 and T_f^0 are the initial coolant and fuel temperatures, respectively, while α_c and α_f represent the coolant and fuel temperature coefficients.

The reactivity data cannot be directly obtained from the Wide Range Nuclear Monitoring System (WRNMS). However, the insertion reactivity can be determined from the control rod position and converted to reactivity values using the rod-worth table. Since each control rod has a different rod worth value, the movement of the four control rods is used to regulate the reactor power level at the desired operating condition. The current reactivity value is computed based on the current rod height and is subsequently converted into a true reactivity value using specific rod worth tables. In other words, each control rod has a different differential reactivity rod worth, and these individual calibration curves were applied prior to determining the total insertion reactivity. These four rods cannot be summed because each rod will hold a different fuel rod.

For the RTP, the coolant temperature coefficient is very small ($\sim 1 \times 10^{-8}$ mΔk/k/°C) and can therefore be neglected (Ribeiro et al., 2020). In addition, the differences between the initial and current coolant and fuel temperatures are assumed to be insignificant. Hence, Equation 9 can be simplified to Equation 10, with the insertion reactivity defined by Equation 11.

$$\rho(t) \approx \delta\rho_{ext}(t) \quad [10]$$

where,

$$\delta\rho_{ext}(t) = \rho_r(t) - \rho_0(t) \quad [11]$$

Here, $\delta\rho_{ext}(t)$ represents the insertion reactivity, defined as the difference between the current reactivity value, $\rho_r(t)$, and the initial reactivity value, $\rho_0(t)$. This simplification indicates that the total reactivity is mainly influenced by changes in the control rod position.

Neutronics Model

The input and output parameters for the neutronics model are the reactivity and neutron values, respectively, as shown in Figure 4. The reactivity is produced by the reactivity model and fed into the neutronics model to generate neutrons. In RTP, the neutrons are detected by a fission chamber and fed into the Neutron Measurement System (NMS). Later, the signals are processed and converted into core power, and the power transformation rate is calculated as the Log Rate. This Log Rate will be utilised to measure the error of the Feedback Control Algorithm (FCA) in controlling the movement of the control rods.

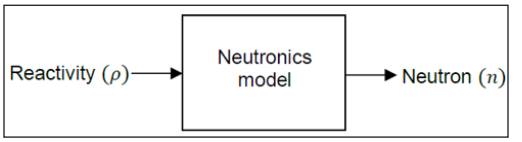

Figure 4. Neutronics subsystem model for RTP

The number of neutrons produced depends on numerous factors, such as the rate of neutron absorption, the fission reaction, the rate of neutron leakage, and the reactor's structural materials. The nuclear fission chain reaction generates neutrons, which will be extinct once they leak outside the reactor or are captured by nuclei. At a certain neutron generation rate, the generated neutrons are absorbed by nuclei, which will trigger fission and produce new neutrons. This is called a delayed neutron. Therefore, the numbers of delayed-neutron precursors and neutrons are used to describe reactor kinetics. The point reactor kinetics equation with six groups of delayed neutron precursors is defined by Equations 12 and 13 (Ribeiro et al., 2020).

$$\frac{dn(t)}{dt} = \left[k_{eff}(1-\beta) - 1\right]\frac{n(t)}{\Lambda} + \sum_{i=1}^{6}\lambda_i C_i(t)\,; \qquad [12]$$

where,

$$i = 1..6,;\ \ \beta = \sum_{i=1}^{6}\beta_i$$

$$\frac{dC(t)}{dt} = k_{eff}\beta_i\frac{n(t)}{\Lambda} - \lambda_i C_i(t) \qquad [13]$$

By referring to Equations 12 and 13, the reactor kinetics can be expressed in simplified forms given by Equations 14 and 15.

$$\frac{dn(t)}{dt} = \frac{\rho(t) - \beta}{\Lambda} n(t) + \sum_{i=1}^{6} \frac{\beta_i}{\Lambda} C_i(t) \quad [14]$$

$$\frac{dC_i(t)}{dt} = C_i n(t) - C_i n_i(t); \;\; i = 1, \ldots, 6 \quad [15]$$

Where n is the number of neutrons, C_i is the number of delayed neutrons precursors in group i, β_i is the delayed neutron fraction of group i, λ_i Is the decay constant for the delayed neutron precursor of the group i, k_{eff} is the effective multiplication factor and Λ is prompt neutron lifetime also called mean neutron generation time. Hence, the actual power can also be known as core power, which is relevant to the neutron density, and the actual core power can be expressed by Equation 16 (Wang et al., 2017).

$$P_a = \psi P_0 \quad [16]$$

where P_a is the actual core power, P_0 is nominal core power and ψ. It is a relative core power.

METHODOLOGY

Data Collection

The real input and output data were acquired at four power levels, i.e., 500kW, 750kW, and 1000kW. The data was recorded for up to 10,000 seconds only because it was sufficient for the RTP system to be completed within that period. Normally, at the beginning, the control rods of RTP were set to an initial height of 220 mm, except for the Regulator rod. When the power reached 15W to get the core excess value, the rods' movement was paused. The rod movement relies strictly on the natural operational and standard control rod manoeuvres required to achieve steady-state power demands (250kW, 500kW, 750kW, and 1000kW). This includes initialising rod heights to 220mm, pausing at 15W, and utilising the auto control system to reach the final power level. No intentional pseudo-random binary sequences or step tests were injected during the operational and data collection.

Before the data were tested, the real initial height of each control rod was identified. Even though the Reactor Digital Instrumentation Control System (ReDICS) in the RTP system sets the initial values for the Shim, Transient, and Safety rods at 220mm, the absolute rod heights differ due to adjustments to control rod movements. The actual initial height of each rod at all power levels is shown in Table 1.

All parameters of the core reactor system were acquired by WRNMS and stored in a computer. According to ReDICS, there are 342 parameters in the RTP system's data acquisition system. The parameters for each subsystem reactor system were intermingled

Table 1
Initial height for each rod

Power level	Initial height level (mm)			
	Shim	Safety	Regulator	Transient
500kW	200.6	200.0	294.5	200.4
750kW	199.6	200.3	233.9	199.5
1000kW	197.6	198.0	197.6	197.8

in the same document. For safety purposes, the data for each variable were recorded redundantly and alternately in the two systems in the same document. 10000 data samples were recorded for each parameter, with a sampling interval of 0.5 seconds. During the preprocessing phase, the data were resampled to a 1-second period, resulting in a refined dataset of 5000 data points for the identification modelling.

System Identification Modelling

Since the model is a black-box model structure, no previous knowledge is required. The Transfer Function (TF) model has been employed in this research to represent all subsystem models using the SI approach. The output of the SI modelling is a transfer function, also called a model, for each subsystem, representing the relationship between real input and output data and is unique to each model. The subsystem model of the RTP reactor system is depicted in Figure 5.

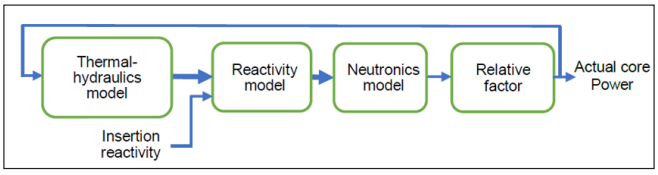

Figure 5. The subsystem model of the RTP reactor system

Since the parameters were in blended data sources, parameter modularisation was needed to categorise each parameter involved in each subsystem model by filtering the data. Then, the data was resampled for a 1-sec period. Therefore, a total of 5000 data points were used in this study, which is adequate to show that the RTP system could be completed within this period. The resampling was done by filtering out duplicate data. However, before analysing, the neutronics model data had to be normalised due to a large gap between the input and output data. The Min-Max Normalisation is expressed in Equation 17 (Chen, 2019).

$$u_i = \frac{[y_i - y_{min}]}{[y_{max} - y_{min}]} \qquad i = 1,2,3,..n \qquad [17]$$

Where u is the output after normalisation, y. Is it a real plant data set or an actual value, *i* is the number of data points until n. The total number of samples. Both datasets were normalised in the range of [0, 1]. The preprocessing flow in SI modelling is shown in Figure 6.

All data were in the time domain and were analysed after the spectra and time were plotted. Subsequently, the means for each data set in the preprocessing operations were removed. The mean value was removed by subtracting the mean value of all the input and the output data, as the Equation 18.

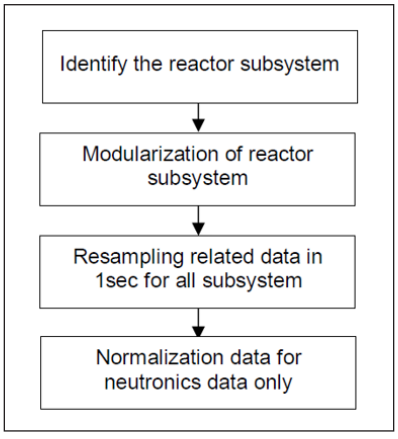

Figure 6. Preprocessing in SI modelling

$$y(t) = u(t) - \bar{u}(t) \quad [18]$$

where $u(t)$ is the input of the system and $\bar{u}(t)$ is the mean input of the system.

The aim of the operations is to obtain more accurate models, since arbitrary variations between input and output data cannot be captured by linear models. In other words, it is a method of data filtering. The data sets ranged between [1 2000].

In the estimation process, the poles and zeros were evaluated up to the 10th order, and the best-fit result was chosen. The best fit (%) quantifies the accuracy of the simulated output in tracking the measured real plat data. The metric represents the Normalised Root Mean Square Error (NRMSE) fit percentage, which normalises the prediction error by the variance of the true data. A value of 100% indicates a perfect match between the model and the actual system. The lower percentages indicate the presence of residual mismatches. The NRMSE (Best fit (%)) is defined in Equation 19 (Ljung, 1999);

$$\text{Best fit (\%)} = 100 \times \left[1 - \frac{\sqrt{\sum_{i=1}^{n}(y_i - \hat{y}_i)^2}}{\sqrt{\sum_{i=1}^{n}(y_i - \bar{y}_i)^2}}\right] \quad [19]$$

Where y_i, is the real plant data (actual value), $\hat{y}_i$ is the predicted model output, $\bar{y}_i$ is the mean of the real plant data, n is the total number of the sample.

For parameter estimation, the covariance matrix of the estimated parameter vector was used to quantify uncertainty in properties such as poles and zeros, as well as in Bode

plots. For the validation process, Akaike's Final Prediction Error (FPE) was used to select the model order. The best fit produced the smallest FPE, as defined in Equation 20 (Roy et al., 2021).

$$\mathrm{FPE} = \frac{1 + d_\gamma/n}{1 - d_\gamma/n} \frac{1}{N} \sum_{t=1}^{n} \frac{1}{2} \varepsilon^2\left(t, \hat{\vartheta}\right) \quad [20]$$

where d_γ is the dimension of the model parameter vector, $\varepsilon(t)$ is the prediction error or residual, ϑ is the parameter vector, and n is the total amount of data.

The smallest FPE evaluated is defined as the estimated model that best matches the real plant, i.e., the most accurate model. The whole process, from identifying each reactor subsystem to modelling validation of the data, has been performed for all reactor subsystems. To provide further justification, the validation process included residual analysis to assess the estimated model's accuracy. The flow of the SI modelling process is depicted in Figure 7.

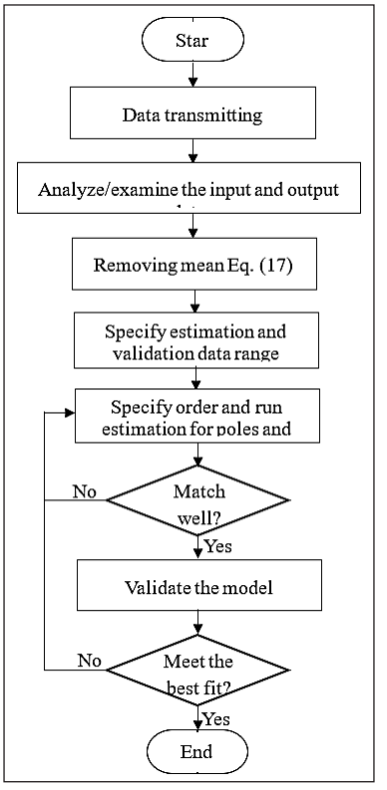

Figure 7. The flow process of SI modelling

The SI model for three subsystems, i.e., the thermal-hydraulics model, reactivity model, and neutronics model, was examined, with all results and plots, including best-fit, poles and zeros, FPE, residual, and RMP between Real Plant (RP) and SI, along with the FP model. The accuracy of the models was also evaluated through Mean Squared Error (MSE). The RMP and MSE are defined in Equations 21 and 22, respectively (Li et al., 2021).

$$\mathrm{RMP} = \left(\frac{y_i - \hat{y}_i}{y_i}\right) \times 100\% \quad [21]$$

$$\mathrm{MSE} = \frac{1}{n} \sum_{i=1}^{n} (y_i - \hat{y}_i)^2 \quad [22]$$

Where y. Is it a real plant data set or an actual value, and $\hat{y}$ is a prediction data set, and i is the number of data points until n. The total number of samples.

RESULTS OF SYSTEM IDENTIFICATION MODEL

There were three subsystems of the reactor core system after modularisation and identification. As mentioned, these subsystems were tested at the specified power level and initial height after resampling for a 1-sec period. Generally, in SI modelling, after analysing the input and output data, the mean is removed, and then the ranges of the estimation and validation values are determined. Since removing means had been done, the pre-processing utilised zeroth-order detrending to eliminate the steady-state direct current (DC) offset, allowing the model to capture the transient variations. This work did not apply the first-order linear detrending. Therefore, any slow drifts due to xenon poisoning or sensor calibration shifts were not mathematically removed. Instead, these variations were left naturally embedded within the operational dataset.

Then, after specifying the order and running pole-and-zero estimation, model validation continues until the best-fit FPE and MSE are met. The figure of the real plant and the SI model was plotted and showed based on FPE, MSE and the best fit of the process. These figures are exposed in Figure 8.

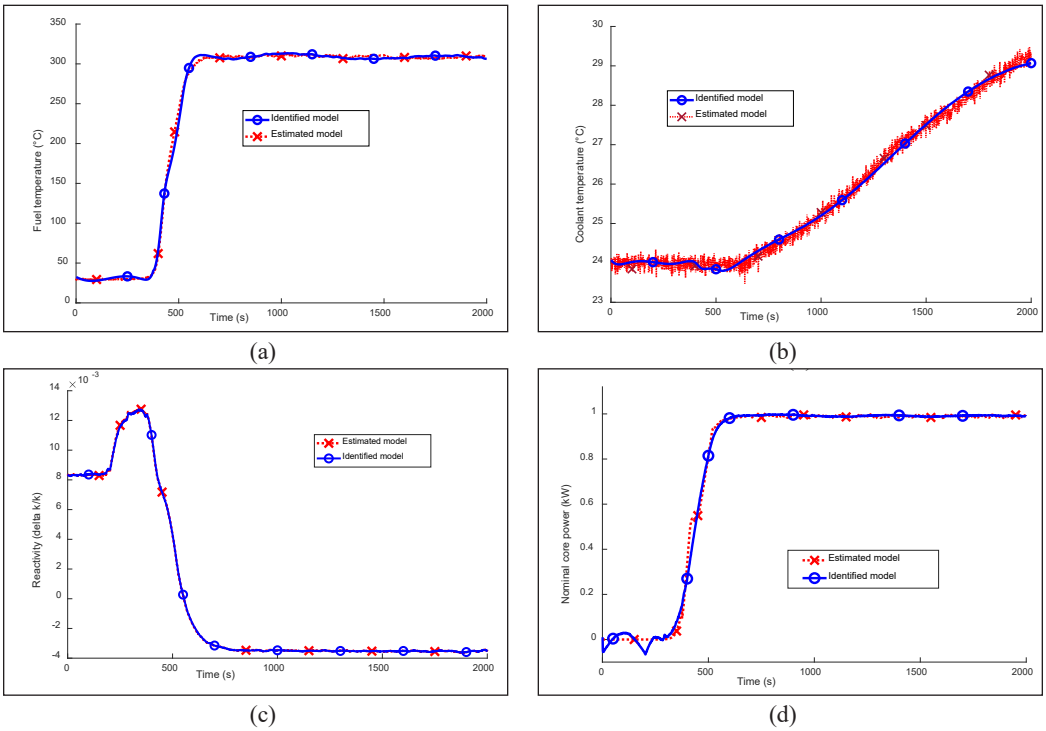

Figure 8. SI and real plant model for (a) fuel temperature of the thermal-hydraulics model, (b) coolant temperature of the thermal-hydraulics model, (c) reactivity model and (d) neutronics model

Generally, the SI model of fuel temperature in thermal-hydraulics, reactivity, and neutronics closely follows the real plant, except during the first hundred seconds in the neutronics model. Figure 8(a) The SI model for fuel temperature of the thermal-hydraulics model can follow the real plant model. The slightest difficulty in tracking from 500sec to 600sec due to strong negative temperature feedback from the reactor core. Thus, core power control performance at RTP shows non-smooth control around 500kW. As shown in Figure 8(b), the SI model of coolant temperature struggles to track the real plant model due to fluctuations in the real plant coolant temperature throughout the process. Furthermore, instead of the actual inlet temperature, a value of 32˚C was utilised due to the absence of inlet water temperature in the WRNMS data acquisition. Compared to others, the SI model of reactivity is the closest to the real plant, as shown in Figure 8(c). Figure 8(d) depicts the SI model of neutronics towards a real plant. For the first 400 seconds, the SI model appears to struggle to track the real plant. This is because the fission reaction is insignificant (the power level is around 25W) at this moment, and the coolant temperature affects it.

In a research reactor, when the coolant temperature is lower, the temperature gradient between the fuel and the coolant is higher. This increased temperature difference enhances the convective heat transfer, allowing more heat to be extracted from the fuel. As a result, the coolant temperature rises as it absorbs the heat from the fuel, while the fuel temperature decreases. This relation is shown in Figure 8, as coolant temperature is increasing in parallel with fuel temperature for both SI and the real plant model and interrelated as also depicted in Equation 6and Equation 7. The best fit, FPE and MSE for each model of the reactor core system are depicted in Table 2 below.

From Table 2, all SI models achieved a best fit above 95%, except for the coolant temperature model in the thermal-hydraulics system, which achieved 92.79%. Models with a best fit exceeding 95% indicate that the SI models are acceptable and can be considered nearly identical to the real plant behaviour. Achieving a better fit for the coolant temperature SI model was challenging due to fluctuations in the actual plant coolant temperature data throughout the process. Nevertheless, the SI models for both fuel and coolant temperatures in the thermal hydraulics system produced relatively similar results, with MSE values of approximately 6.773 and 6.873 and FPE values of 0.257 and 0.267, respectively. These values are larger compared to those obtained for the reactivity and neutronics SI models.

Table 2
SI modelling evaluation

Model	Best fit (%)	FPE	MSE
Fuel temperature for thermal hydraulics	96.62	0.257	6.773
Coolant temperature for thermal hydraulics	92.79	0.267	6.873
Reactivity	99.31	4.502E-9	1.892E-9
Neutronics	95.66	1.657E-4	1.618E-4

The SI models of reactivity and neutronics exhibit insignificant FPE and MSE values, with the reactivity SI model achieving the highest best fit of 99.31%. This demonstrates that the reactivity model most accurately represents the behaviour of the real plant. In addition, both the fuel-temperature and coolant-temperature models were developed using second-order transfer functions. The SI approach successfully generated a transfer function for each model. The resulting transfer functions for the thermal-hydraulics models of fuel temperature and coolant temperature are presented in Equations 23 and 24, respectively.

$$T_f = \frac{2.514s^2 + 0.1122s + 8.076e^{-5}}{s^2 + 2.3831e^{-2}s + 2.973e^{-6}} \quad [23]$$

$$T_c = \frac{377.1s + 189.6}{s^2 + 10.48s + 0.5157} \quad [24]$$

The reactivity model calculates the total reactivity of the reactor system by summing the insertion and feedback reactivities arising from fuel and coolant temperatures. After the SI modelling stage, the best-fit reactivity model achieved 99.31% with 4.502E-9 FPE, as shown in Table 2. The transfer function results for the reactivity model represent the insertion reactivity due to control rod movement, feedback reactivity due to fuel temperature, and feedback reactivity due to coolant temperature, as presented in Equations 25, 26, and 27, respectively.

Insertion reactivity due to control rod motion

$$\rho_{ext}(t) = \frac{2.409s + 8.816e^{-4}}{s^2 + 2.449s + 8.97e^{-4}} \quad [25]$$

Feedback reactivity due to fuel

$$\rho_f(t) = \frac{-8.08e^{-5}s - 5.092e^{-4}}{s + 5.908} \quad [26]$$

Feedback reactivity due to the coolant

$$\rho_c(t) = \frac{3.895e^{-5}s + 1.714e^{-8}}{s + 3.164e^{-4}} \quad [27]$$

For nominal core power, the input-output relationship was between reactivity and nominal core power. Based on the rods' movement, the reactivity model produced a reactivity value, which was utilised in the neutronics model to determine the nominal core

power, before being converted to the actual core power. The model for nominal core power from neutrons in the SI technique is given by Equation 28.

$$P_0 = \frac{1485.45^2 + 64.667075s + 21.75}{1537s^2 + 1542s + 5} \quad [28]$$

Analysis Results of the Thermal-Hydraulics Model

Figure 9 illustrates the fuel and coolant temperature responses of the thermal-hydraulics model at different power levels, namely 500kW, 750kW, and 1000kW. Starting from

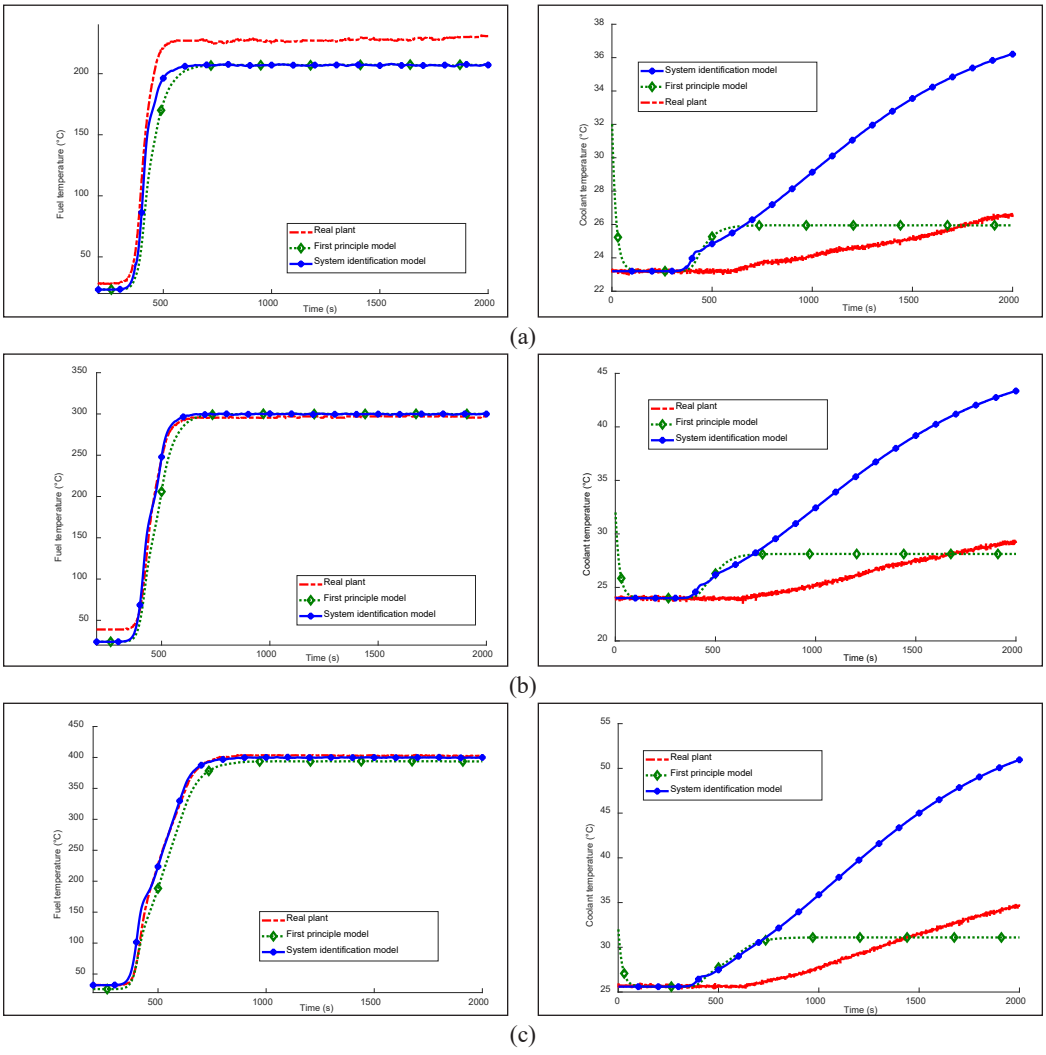

Figure 9. Fuel and coolant temperature responses of the thermal-hydraulics model at (a) 500kW, (b) 750kW, and (c) 1000kW

approximately 26°C, the fuel temperature increases with increasing power level and reaches nearly 300°C. The figures show that both the SI and FP models for the 500kW data set have difficulty accurately tracking the actual plant fuel temperature, exhibiting large steady-state deviations. However, as the power level increases, both models become better at following the real plant fuel temperature response. In particular, the fuel temperature responses at 750kW and 1000kW demonstrate that the SI model provides the best representation of the reactor system fuel temperature.

In contrast, the coolant temperature responses for all data sets and power levels do not closely follow the real plant coolant temperature. The figures indicate that the SI model predicts a gradual increase in coolant temperature to nearly twice the real plant response. Meanwhile, the FP model can control the initial increase in coolant temperature before maintaining it at a relatively constant value.

It is evident that the coolant temperature responses of both the SI and FP models deviate from the real plant behaviour. In this study, a fixed inlet coolant temperature of 32°C was used in the thermal-hydraulics model due to the lack of real-time inlet coolant temperature data. As a result, modelling coolant temperature becomes more challenging and may lead to inaccuracies in the model's response. Therefore, the inlet coolant temperature model requires further investigation and improvement. In addition, the coolant temperature coefficient ($\sim 1 \times 10^{-8}$ mΔk/k/°C) is insignificant compared to the fuel temperature coefficient (-0.1 mΔk/k/°C) (Minhat et al., 2018). Hence, the deviation in coolant temperature does not significantly affect the reactor core system power level.

Table 3 summarises the mean and RMP values of fuel temperature for the reactor system, using real plant data, the FP model, and the SI model. The results indicate that at the 500kW power level, both the SI and FP models have difficulty accurately tracking the real plant fuel temperature, as shown by the considerable RMP differences relative to other power levels. However, as the power level increases, the RMP values decrease, indicating that both the SI and FP models are better able to follow the real plant behaviour.

Table 3
Mean and RMP based on real plant data for fuel and coolant temperature

Power Level (kW)	Mean temperature, (°C)			RMP (%)	
	Real plant	FP model	SI model	FP	SI
Fuel Temperature					
500	204.216	181.902	184.596	10.93	9.61
750	259.625	257.388	261.438	0.86	-0.69
1000	338.852	326.399	331.809	3.68	2.08
Coolant Temperature					
500	24.347	25.401	29.207	-4.33	-19.96
750	25.796	27.184	32.712	-5.38	-26.81
1000	28.702	29.662	36.580	-3.35	-27.45

Several negative RMP values were also observed, indicating that the predicted values from the FP and SI models exceeded the corresponding real plant values. As illustrated in Figure 9 for the 750kW fuel temperature response, the SI model is slightly lower than the real plant during the first 300sec but subsequently becomes noticeably higher than the real plant response. This deviation may be attributed to the increasing reactor power level, which affects the thermal behaviour of the reactor core and introduces nonlinear characteristics that the SI model finds difficult to capture accurately. In addition, uncertainties in heat transfer parameters and coolant flow behaviour may contribute to the observed differences between the model and the plant's actual response.

Analysis Results of the Reactivity Model

Plotted graphs comparing the SI, FP, and real plant reactivity models are shown in Figure 10 for all power levels. In all cases, the FP model closely follows the real plant response up to approximately 300sec; however, it subsequently decreases and stabilises at near-zero reactivity, deviating significantly from the real plant's total reactivity. In contrast, the SI model can track the real plant behaviour more consistently across all power levels.

From the figures, the SI reactivity model at all three power levels exhibits a trend similar to the real plant: both initially increase to approximately 4×10^{-3} delta k/k, then decrease

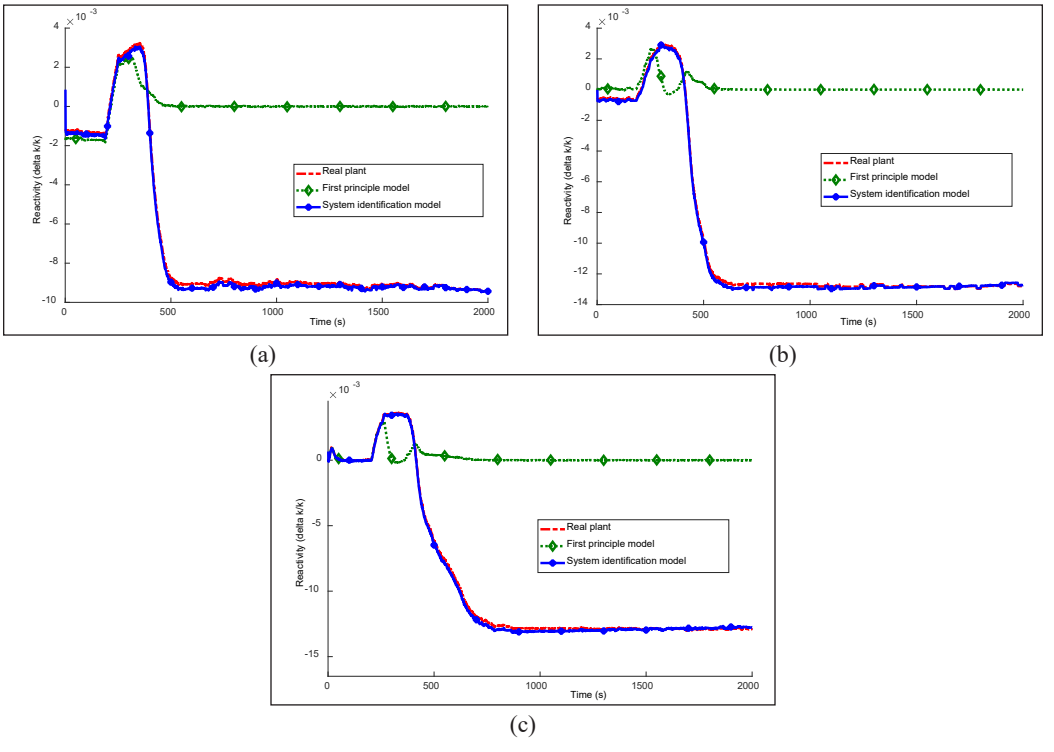

Figure 10. Total reactivity values at (a) 500kW, (b) 750kW, and (c) 1000kW

and stabilise at a negative reactivity level. For the 500kW case, the system stabilises at approximately -9×10^{-3} delta k/k. Similarly, for 750kW and 1000kW, the total reactivity stabilises at around -13×10^{-3} delta k/k and -14×10^{-3} delta k/k, respectively. However, at 500kW, the SI model shows a slight deviation from the real plant between 500sec and 900sec. This variation may be attributed to temperature feedback effects on reactivity, in which temperature changes influence neutron absorption behaviour and introduce modelling uncertainties under transitional operating conditions.

As shown in Table 4, the comparison of mean values and RMP for the reactivity models at each power level is presented. Although some RMP values are negative, the results indicate that the SI model consistently provides closer agreement with the real plant than the FP model, as reflected in its lower RMP values. The SI model RMP ranges from |1.09%| to |1.84%|, which is significantly smaller than that of the FP model, which ranges from 101.37% to 102.31%.

Table 4
Mean and RMP values of total reactivity based on real plant data

Power Level (kW)	Reactivity, ρ(Δk/k)			RMP (%)	
	Real plant	FP model	SI Model	FP model	SI Model
500	-7.685E-03	1.779E-04	-7.826E-03	102.31	-1.84
750	-1.062E-02	1.455E-04	-1.073E-02	101.37	-1.09
1000	-1.013E-02	1.601Ee-04	-1.025E-02	101.58	-1.18

Analysis Results of the Neutronics Model

Figure 11 illustrates the plotted responses of the neutronic model at each power level. Overall, the SI model demonstrates closer agreement with the real plant behaviour of the neutronic response across all power levels compared with the FP model. The results show that during the initial 200 seconds, the SI model closely tracks the real plant response. However, a temporary deviation is observed between approximately 200sec and 350sec. After 350 seconds, the SI model gradually converges towards the real plant trend, although it does not fully match the exact values.

As the power level increases from 500kW to 750kW, the SI model shows improved agreement with the real plant response. However, at 1000kW, a more noticeable discrepancy is observed, indicating reduced modelling accuracy at higher operating conditions. This suggests that the SI model faces greater challenges in capturing the neutronic behaviour at elevated power levels.

The input to the neutronics model is based on the reactor reactivity output. It is observed that when the reactivity increases and subsequently decreases between 250sec and 500sec, the neutronic response exhibits an inverse behaviour. This behaviour may be associated with xenon poisoning effects within the reactor core, which influence neutron absorption

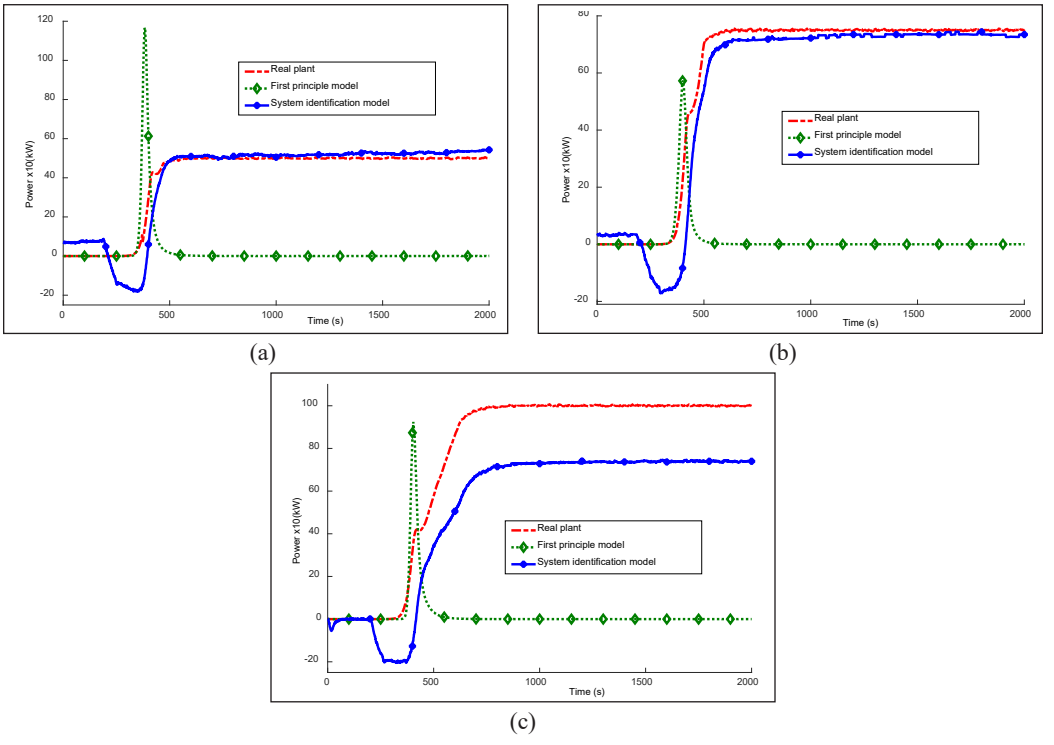

Figure 11. Actual core power response of the neutronics model at (a) 500kW, (b) 750kW, and (c) 1000kW power levels

and reactor kinetics. In contrast, the FP model does not accurately reproduce the real plant behaviour at all power levels. It shows an initial rise, peaking around 500sec, followed by a rapid decline back towards the initial level, and subsequently diverges from the real plant response for the remainder of the simulation.

The analysis for each power level was conducted by calculating the mean and RMP of the SI and FP models using real-plant data. The analysis results presented in Table 5 indicate that the RMP values for the SI models were significantly smaller, remaining below 8% for the 500kW and 750kW power levels. The neutronics model depends on the total reactivity value to produce the nominal core power. However, at the 1000kW power

Table 5
Mean and RMP based on real plant data for the neutronics model

Power Level (kW)	Power (kW)			RMP (%)	
	Real Plant	FP Model	SI Model	FP Model	SI Model
500	444.107	2.633	438.440	99.41	1.28
750	653.497	1.606	605.619	99.75	7.33
1000	843.109	2.265	577.233	99.73	31.54

level, the residual percentage increased to 31.54%. In contrast, the RMP values for all FP models deviated considerably from the real plant data, reaching approximately 99%. Therefore, the SI models outperformed the FP models, producing lower RMP values across all power levels.

CONCLUSION

The modelling approach for all subsystems of the reactor core system involved developing thermal-hydraulic, reactivity, and neutronics models. The evaluation used the highest best-fit value and the lowest FPE and MSE values to assess model accuracy, ensuring that the selected model was like the real plant. The results showed that the fuel temperature of the thermal-hydraulics, reactivity, and neutronics models provided the best fit, with 95% higher than that of the coolant temperature model. The lowest FPE and MSE values came from neutronics and reactivity models. In general, both coolant and fuel temperature models of thermal-hydraulics, as well as insertion reactivity due to control rod motion and neutronics models, produced a second-order model. However, both feedback reactivity due to fuel and coolant had been modelled as first-order. The MSE analysis showed that the reactivity and fuel temperature of the thermal hydraulics of FP models were lower than those of the SI model at all power levels. Meanwhile, the coolant temperature in the SI model's thermal-hydraulics and neutronics sections is lower at all power levels. This indicates that the neutronics and fuel temperature in the SI model's thermal hydraulics are closer to the real plant than those in FP.

ACKNOWLEDGEMENTS

The authors also express their sincere gratitude to the Malaysian Nuclear Agency for providing the data and technical advice that contributed to the successful completion of this research.

REFERENCES

Aguel, S., Meddeb, Z., & Jeday, M. R. (2019). Parametric study and modeling of cross-flow heat exchanger fouling in phosphoric acid concentration plant using artificial neural network. *Journal of Process Control, 84*, 133-145. https://doi.org/10.1016/j.jprocont.2019.10.001

Arda, S. E., & Holbert, K. E. (2016). Nonlinear dynamic modeling and simulation of a passively cooled small modular reactor. *Progress in Nuclear Energy, 91*, 116-131. https://doi.org/10.1016/j.pnucene.2016.03.033

Cammi, A., Ponciroli, R., Borio di Tigliole, A., Magrotti, G., Prata, M., Chiesa, D., & Previtali, E. (2013). A zero dimensional model for simulation of TRIGA Mark II dynamic response. *Progress in Nuclear Energy, 68*, 43-54. https://doi.org/10.1016/j.pnucene.2013.04.002

Chen, P. (2019). Effects of normalization on the entropy-based TOPSIS method. *Expert Systems with Applications, 136*, 33-41. https://doi.org/10.1016/j.eswa.2019.06.035

Dim, O. U., & Aghara, S. K. (2019). Modeling and evaluation of fissile material utilization of the UMLRR using Monte Carlo MCNP6 code. *Annals of Nuclear Energy, 130*, 365–376. https://doi.org/10.1016/j.anucene.2019.03.007

Ghazali, A. K., Minhat, M. S., & Hassan, M. K. (2017). Automated power control system for reactor TRIGA PUSPATI. *AIP Conference Proceedings, 1802*, Article 020010. https://doi.org/10.1063/1.4972908

Kazeminejad, H. (2012). Thermal–hydraulic modeling of reactivity insertion in a research reactor. *Annals of Nuclear Energy, 45*, 59-67. https://doi.org/10.1016/j.anucene.2012.02.017

Khalid, M., & Khan, M. T. (2023). Intelligent fuzzy based fault diagnosis and control techniques for industrial process systems: A review. *Engineering Applications of Artificial Intelligence, 122*, Article 106130.

Kim, B. S., & Kim, T. G. (2020). Modeling and simulation using artificial neural network-embedded cellular automata. *IEEE Access, 8*, 24056–24061. https://doi.org/10.1109/access.2020.2970547

Leong, C., Semiao, J., Santos, M. B., Teixeira, I. C., Teixeira, J. P., Batista, A. J. N., Goncalves, B., & Marques, J. G. (2015). Fast radiation monitoring in FPGA-based designs. In *2015 Conference on Design of Circuits and Integrated Systems (DCIS)* (pp. 1-6). IEEE. https://doi.org/10.1109/dcis.2015.7388590

Li, Q., Ma, Q., Li, Y., Chen, P., Ma, C., Zhao, B., & Chen, H. (2021). Numerical investigation of conjugated heat transfer of the plate-type fuel assembly in the research reactor. *Frontiers in Energy Research, 9*, Article 663533. https://doi.org/10.3389/fenrg.2021.663533

Liu, H., Chen, T., & Qin, S. J. (2024). State space system identification and fault detection for nonlinear industrial processes. *ISA Transactions, 146*, 120-132.

Ljung, L. (1999). *System identification: Theory for the user* (2nd ed.). Prentice Hall.

Mao, X., Song, S., & Ding, F. (2022). Optimal BP neural network algorithm for state of charge estimation of lithium-ion battery using PSO with Levy flight. *Journal of Energy Storage, 49*, Article 104139. https://doi.org/10.1016/j.est.2022.104139

Martón, I., Sánchez, A. I., Carlos, S., Mullor, R., & Martorell, S. (2023). Prognosis of wear-out effect on safety equipment reliability for nuclear power plants long-term safe operation. *Reliability Engineering & System Safety, 233*, Article 109121. https://doi.org/10.1016/j.ress.2023.109121

Melo, A., Câmara, M. M., & Pinto, J. C. (2024). Data-driven process monitoring and fault diagnosis: A comprehensive survey. *Processes, 12*(2), Article 251. https://doi.org/10.3390/pr12020251

Minhat, M. S., Mohd Subha, N. A., Hassan, F., & Mohamad Nordin, N. (2020). An improved control rod selection algorithm for core power control at TRIGA PUSPATI reactor. *Journal of Mechanical Engineering and Sciences, 14*(1), 6362-6379. https://doi.org/10.15282/jmes.14.1.2020.13.0498

Minhat, M. S., Selamat, H., & Mohd Subha, N. A. (2018). Adaptive control method for core power control in TRIGA Mark II reactor. *IOP Conference Series: Materials Science and Engineering, 298*, Article 012028. https://doi.org/10.1088/1757-899x/298/1/012028

Mohindru, P. (2024). Review on PID, fuzzy and hybrid fuzzy PID controllers for controlling non-linear dynamic behaviour of chemical plants. *Artificial Intelligence Review, 57*(4), Article 97. https://doi.org/10.1007/s10462-024-10743-0

Nagai, Y., Hatsukawa, Y., Kin, T., Hashimoto, K., Motoishi, S., Konno, C., Ochiai, K., Takakura, K., Sato, Y., Kawauchi, Y., Sato, N., Ohta, A., Yamabayashi, H., Tanase, M., Fujisaki, S., Teranaka, T., Takeuchi, N., & Igarashi, T. (2011). Successful labeling of 99mTc-MDP using 99mTc separated from 99Mo produced by 100Mo(n,2n)99Mo. *Journal of the Physical Society of Japan, 80*(8), Article 083201. https://doi.org/10.1143/jpsj.80.083201

Nguyen, N.-D., Nguyen, K.-C., Huynh, T.-N., Vo, D.-H.-D., & Tran, H.-N. (2020). Conceptual design of a 10 MW multipurpose research reactor using VVR-KN fuel. *Science and Technology of Nuclear Installations, 2020*, Article 7972827. https://doi.org/10.1155/2020/7972827

Oka, Y., & Suzuki, K. (Eds.). (2013). *Nuclear reactor kinetics and plant control*. Springer. https://doi.org/10.1007/978-4-431-54195-0

Ratiko, R., Wisnubroto, D. S., Nasruddin, N., & Mahlia, T. M. I. (2020). Current and future strategies for spent nuclear fuel management in Indonesia. *Energy Strategy Reviews, 32*, Article 100575. https://doi.org/10.1016/j.esr.2020.100575

Ribeiro, E. R. G. D., Palma, D. A. P., Henrice, E., Jr., & Su, J. (2020). Transient analysis of the Brazilian Multipurpose Reactor by the coupled neutronics and thermal hydraulics code NTHC1. *Annals of Nuclear Energy, 143*, Article 107449. https://doi.org/10.1016/j.anucene.2020.107449

Roy, D. K., Biswas, S. K., Saha, K. K., & Murad, K. F. I. (2021). Groundwater level forecast via a discrete space-state modelling approach as a surrogate to complex groundwater simulation modelling. *Water Resources Management, 35*(6), 1653-1672. https://doi.org/10.1007/s11269-021-02787-6

Safaei Arshi, S., Amin Mozafari, M., Jozvaziri, A., & Mirvakili, S. M. (2021). Investigation of safety aspects during steady state operation of Tehran research reactor fuel test loop. *Progress in Nuclear Energy, 140*, Article 103895. https://doi.org/10.1016/j.pnucene.2021.103895

Son, S. H., Kim, J. W., Oh, T. H., Jeong, D. H., & Lee, J. M. (2022). Learning of model-plant mismatch map via neural network modeling and its application to offset-free model predictive control. *Journal of Process Control, 115*, 112-122. https://doi.org/10.1016/j.jprocont.2022.04.014

Tang, H. H., & Ahmad, N. S. (2024). Fuzzy logic approach for controlling uncertain and nonlinear systems: A comprehensive review of applications and advances. *Systems Science & Control Engineering, 12*(1), Article 2394429. https://doi.org/10.1080/21642583.2024.2394429

Wang, G., Wu, J., Zeng, B., Xu, Z., Wu, W., & Ma, X. (2017). State-space model predictive control method for core power control in pressurized water reactor nuclear power stations. *Nuclear Engineering and Technology, 49*(1), 134-140. https://doi.org/10.1016/j.net.2016.07.008

Wang, Y., Zhao, C., & Huang, B. (2024). Data-driven dynamic modelling and system identification for nonlinear industrial process monitoring. *Chemical Engineering Research and Design, 204*, 215-228.

Wu, Z., Christofides, P. D., Wu, W., Wang, Y., Abdullah, F., Alnajdi, A., & Kadakia, Y. (2025). A tutorial review of machine learning-based model predictive control methods. *Reviews in Chemical Engineering, 41*(4), 359-400. https://doi.org/10.1515/revce-2024-0055

Zhang, X., Gao, Z., & Jiang, Q. (2025). Dynamic system identification and predictive modelling for complex industrial systems using data-driven approaches. *Computers & Chemical Engineering, 188*, Article 108771.